Supporting Information

Switching Ultra-Stretchability and Sensitivity in Metal Films for Electronic Skins: A Pufferfish-Inspired, Interlayer Regulation Strategy

Tianming Sun‡[a,b], Bin Feng‡[b], Jinpeng Huo[b], Yu Xiao[b], Jin Peng[b], Zehua Li[b], Wengan Wang[b], Lei Liu[b], Guisheng Zou[,b], Wenxian Wang*[,a]*

[a] College of Materials Science and Engineering, Taiyuan University of Technology, Taiyuan 030024, Shanxi Province, China.

[b] Department of Mechanical Engineering, State Key Laboratory of Tribology, Key Laboratory for Advanced Manufacturing by Materials Processing Technology, Ministry of Education of PR China, Tsinghua University, Beijing 100084, P. R. China.

*Corresponding author. E-mail address: wangwenxian@tyut.edu.cn; zougsh@tsinghua.edu.cn

‡ These authors contributed equally to this work.

The PDF file includes:

Notes S1 to S3

Figures S1 to S12

Table S1

References

Supporting Notes

Note S1. The gauge factor (GF) of the proposed metal films

In the field of strain sensors, sensitivity, as one of the important indexes to evaluate the electromechanical performance of the sensors, is defined as the gauge factor (GF=($\Delta R/R_0$)/ε), where ΔR is the resistance change in the strain state, R_0 is the initial resistance of the film before strain and ε is the applied strain. In fact, the resistance change vs strain displays a curved shape rather than a single straight line. Therefore, the most common method to calculate the GF is to approximately divide the sensing curve into several quasilinear stages. Among all stages of GF, the stage with maximum GF is usually considered to reflect the sensitivity of the sensors.

Note S2. The elucidation of deposition pressure-tunable surface roughness in the interlayer.

In the physical deposition process, deposition pressure is an important parameter. As the deposition pressure increases, more nano/micro-voids are induced in the deposited FeO_X interlayer, accompanied with an increase in the surface area of the film (Fig. S6, ESI†). Therefore, the surface roughness of the FeO_X interlayer also gradually increases, as shown in Fig 4a, b, and Fig S7 (ESI†). The mechanism of this deposition pressure-induced regulation may involve a series of processes such as collisions, scattering, excitation, and chemical reactions between the ejected atoms from the laser-ablated target and gas atoms during the physical deposition[1]. To date, the effect of the deposition pressure on the morphology of deposited products has not been systematically studied. Several possible reasons were proposed to jointly elucidate the increased surface roughness at higher deposition pressures. First, compared with the vacuum environment, there is a higher possibility for the atoms ejected from the target to collide with gas molecules in a higher-pressure environment, resulting in significantly less kinetic energy for the atoms when reaching the substrate. This effect means that the deposited atoms lack sufficient energy to further migrate on the substrate to form a smooth, compact film[2,3]. Therefore, the surface roughness of the interlayer is increased at higher deposition pressures. Second, high-frequency collisions of ejected atoms from the target with gas atoms lead to more random scattering of atoms in the higher-pressure environment due to the smaller mean free path[1,4]. This enhanced atom scattering can facilitate the formation of massive voids by inducing a disordered atom stacking, leading to an increase in the surface roughness of the interlayer.

Note S3. The concept of the normalized parameters of crack density and cut-through proportion

The normalized parameters of crack density and cut-through proportion were used to analyze the features of the crack pattern of the proposed metal films with the different surface roughness interlayers under 90% strain in Fig. 2c. The samples deposited at 0.5 Pa with a surface roughness of 0.047 μm were set to the base level. Crack density is the number of cracks in the whole image. Cut-through proportion is defined as the ratio of the number of cut-through cracks to the total number of cracks.

Supporting Figures

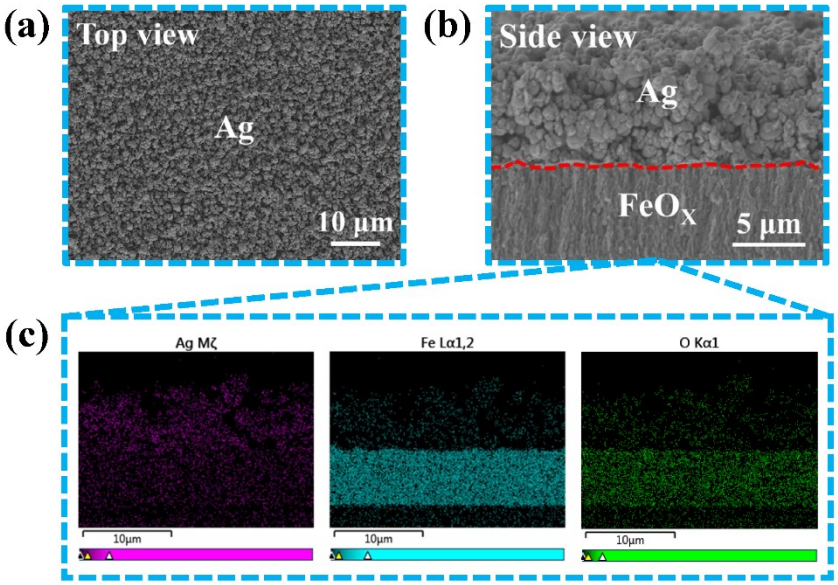

Fig. S1. The surface morphology and composition characterization of the as-fabricated metal films. (a) The top view SEM image, (b) The side view SEM image, (c) The EDS composition analysis.

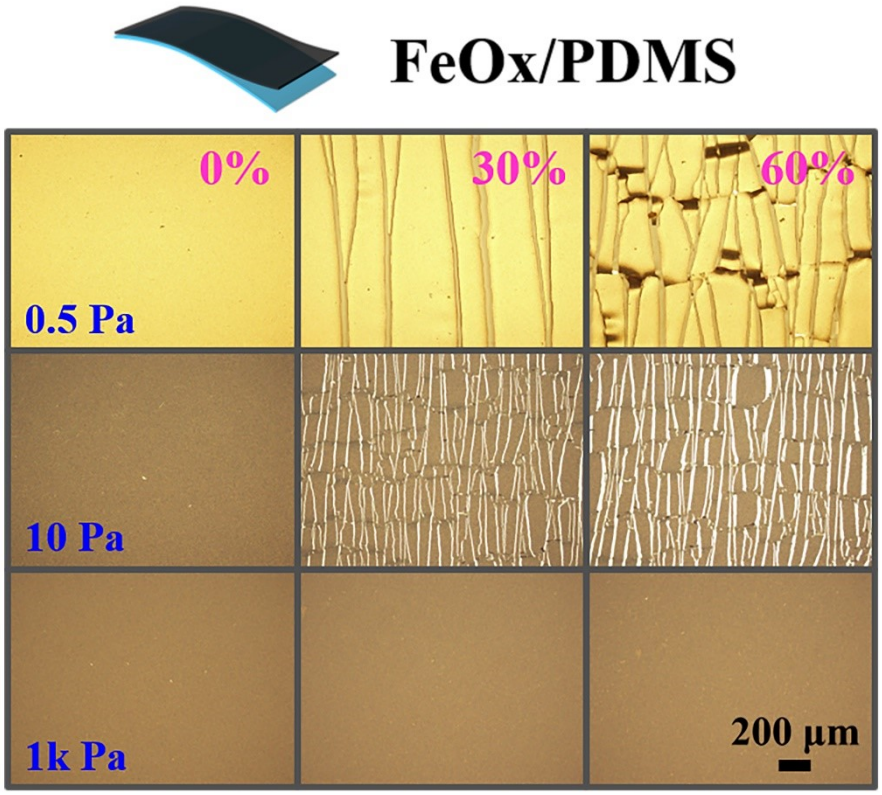

Fig. S2. The strain-dependent surface morphology evolution of the FeO_X interlayer deposited at various pressures (0%, 30%,60%).

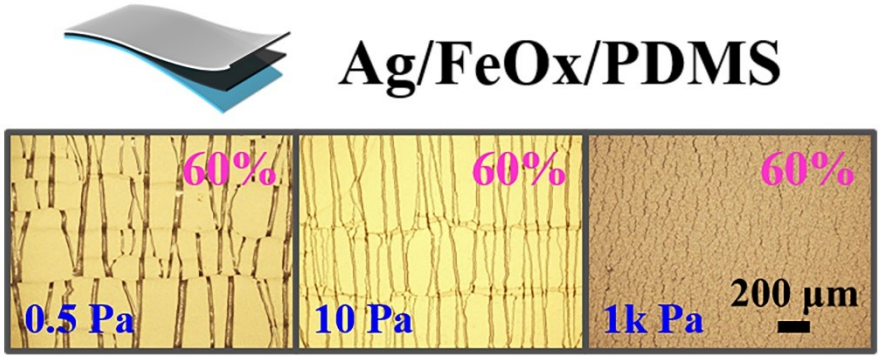

Fig. S3. The surface morphology evolution of the metal films under 60% strain after the introduction of the FeO_X interlayer deposited at various pressures

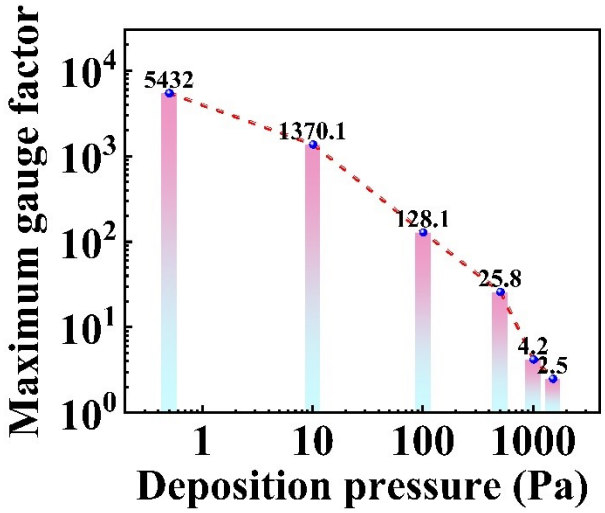

Fig. S4. The maximum sensitivity gauge factor (GF) of the proposed metal films with the deposition pressure of the FeO_X interlayer.

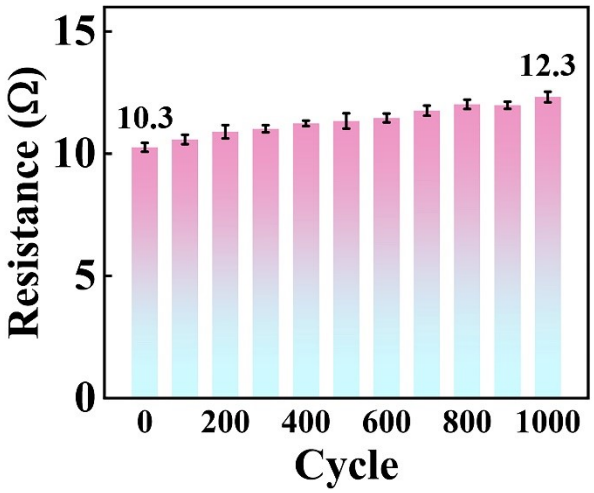

Fig. S5. The initial resistance of the ultra-stretchable metal films after the repeated cycling test under 100% strain.

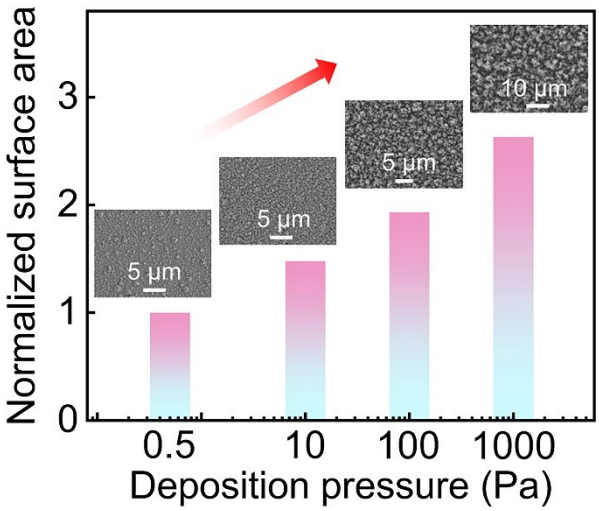

Fig. S6. The normalized surface area of the FeO_X interlayer at different deposition pressure. Inset: SEM images of the FeO_X interlayer at different deposition pressure.

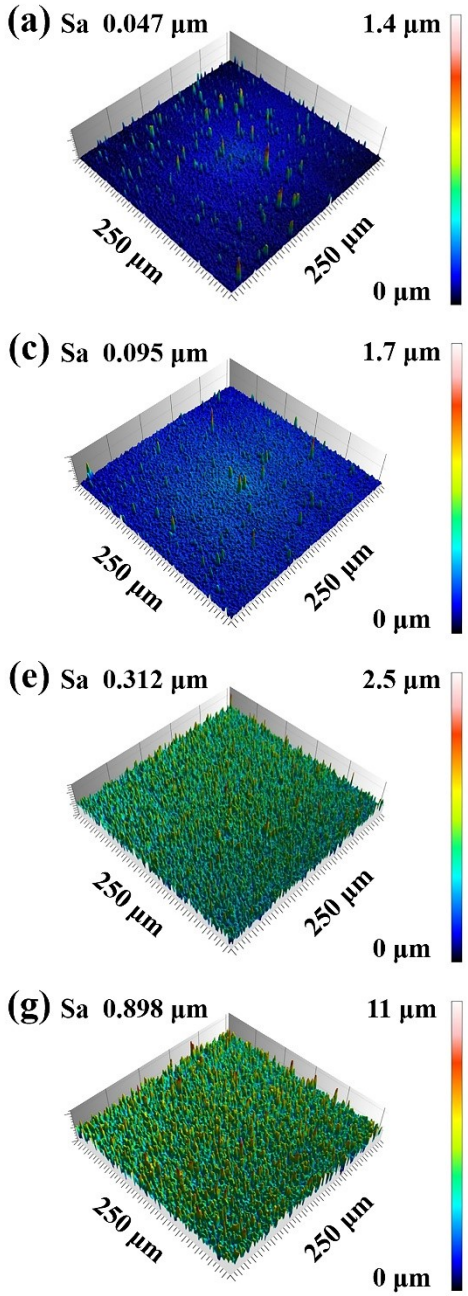

(b)			
Sq	0.07841	µm	
Ssk	3.557		
Sku	21.05		
Sp	0.8918	µm	
Sv	0.1671	µm	
Sz	1.059	µm	
Sa	0.04694	µm	

(d)			
Sq	0.1314	µm	
Ssk	1.541		
Sku	9.935		
Sp	1.293	µm	
Sv	1.042	µm	
Sz	2.336	µm	
Sa	0.09471	µm	

(f)			
Sq	0.3981	µm	
Ssk	0.6243		
Sku	3.730		
Sp	2.272	µm	
Sv	1.736	µm	
Sz	4.008	µm	
Sa	0.3121	µm	

(h)			
Sq	1.130	µm	
Ssk	0.4896		
Sku	3.312		
Sp	5.531	µm	
Sv	3.446	µm	
Sz	8.977	µm	
Sa	0.8981	µm	

Fig. S7. The surface roughness and corresponding physical parameters of the various FeO_X interlayer (Fig. 4a) characterized by a laser scanning confocal microscope.

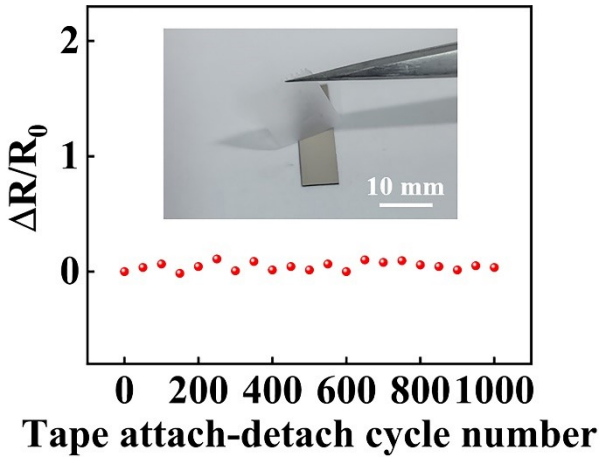

Fig. S8. The relative resistance changes ($\Delta R/R_0$) of the proposed metal films during the repeated tape attachment/detachment.

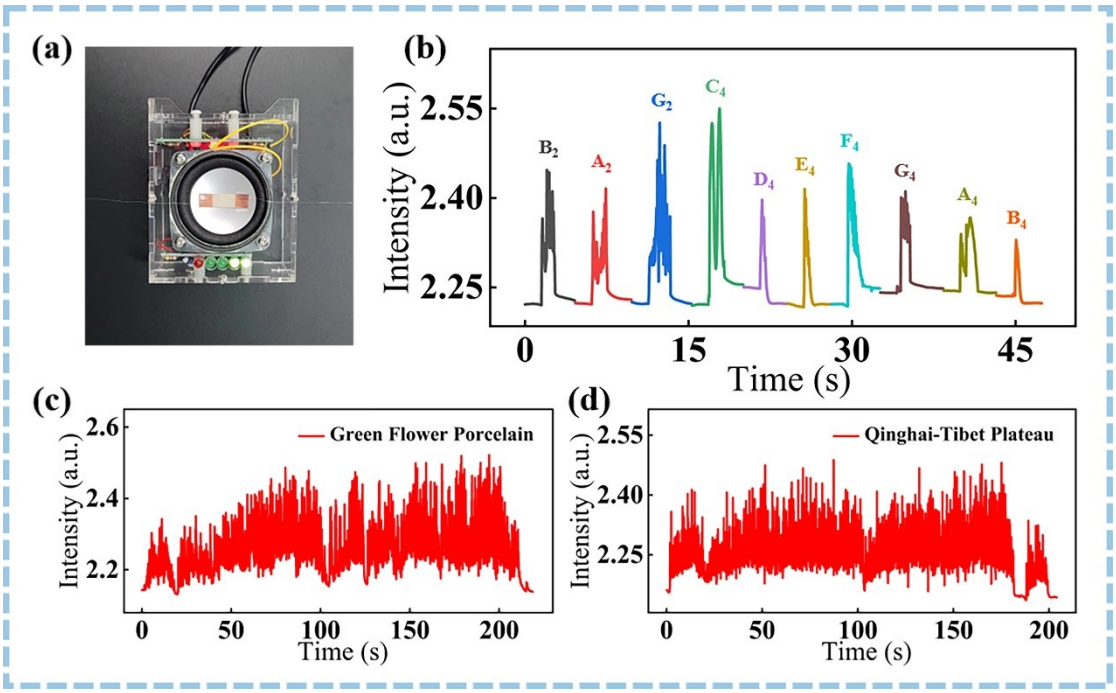

Fig. S9. The high-sensitive metal film-based strain sensors are used to detect sound vibrations. (a) Image of the sensor attached to the speaker. (b) The waveform profiles of the various piano tones collected from the speaker. (c) and (d) The continuous waveforms for the music of “Green Flower Porcelain” and “Qinghai-Tibet Plateau”, respectively.

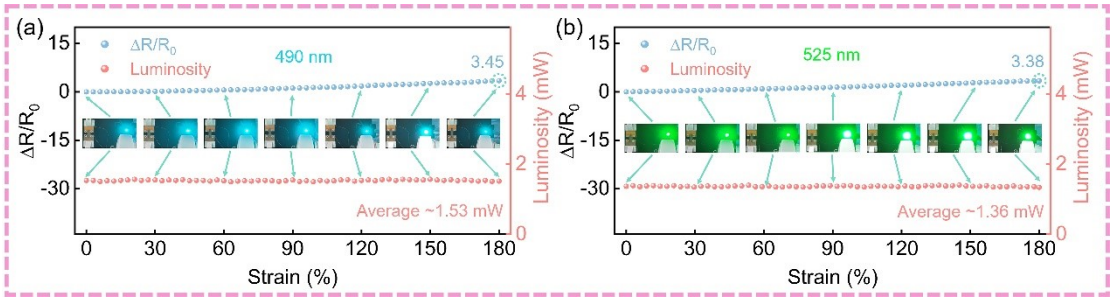

Fig. S10. The relative resistance change ($\Delta R/R_0$) of the sensor and the luminosity of the LED (λ: 490 nm and 525 nm) varying with the applied strain (0~180%)

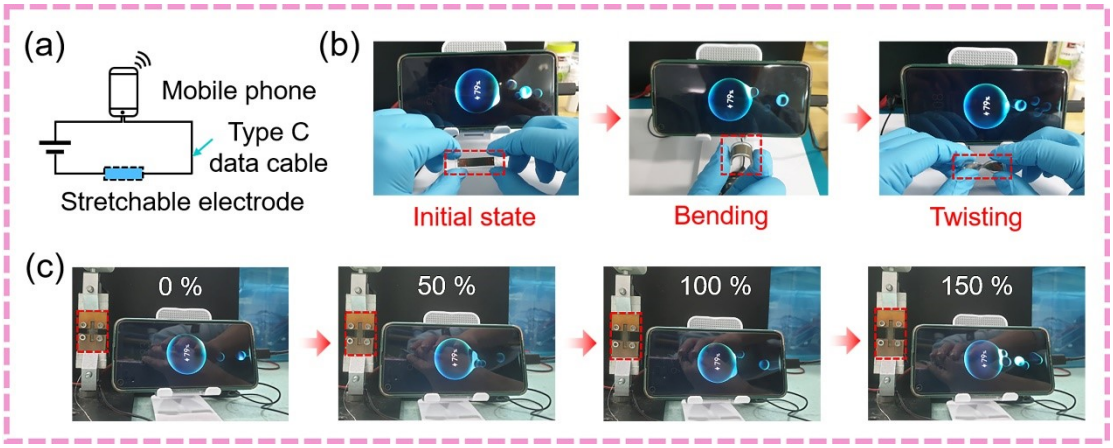

Fig. S11. The ultra-stretchable metal film serves as a component of the Type C data cable for the mobile phone charging process. (a) Schematic of the whole circuit. The ultra-stretchable metal film was connected in series with the mobile phone as a component of the Type C data cable. (b) Digital image of the mobile phone charging process when the proposed metal film is subjected to a series of actions (initial state, bending, and twisting). (c) Digital image of the mobile phone charging process when the proposed metal film is subjected to a certain strain (0~150%).

Fig. S12. Photograph of wide-range metal film-based strain sensors attached to five fingers.

Supporting Table

Table S1. The summary of the electromechanical performance of the typical crack-based flexible strain sensors reported in previous works.

Design strategy	Maximum stretchability	$\Delta R/R_0$ at ε_{max}	Tunable stretchability	References
Spider-inspired nanoscale crack junction	2%	45	0~2%	[5]
Introduction of parallel graphene	10%	10	1%, 10%	[6]
2D-material interlayer insertion	24%	10000	6~24%	[7]
Substrate structuring	60%	100	30~60%	[8]
Fusion of layered membrane-interface-elastomer structure	85%	100	15%, 85%	[9]
Nanosphere lithography-based strategy	90%	150	5%, 90%	[10]
Spiral structure-controlled cracking	100%	5	80%, 100%	[11]
Geometrical modulation	100%	25	3~100%	[12]
Film wrinkling	110%	75	40~110%	[122]
Surface chemistry modification	120%	34	0~120%	[14]
Thickness-Gradient Films	150%	32	150%	[15]
Microcrack bridging	200%	45	8~200%	[16]
One-step defect-implantation	200%	2.5	20~200%	[17]
Substrate thermal expansion	300%	100	17%, 300%	[18]
Interlayer regulation strategy	**0~295%**	**3.85**	**11~295%**	**This work**

Supporting References

1 O. V. Devitsky, Ekaterinburg, Russia, 2022, p. 030002.
2 Marta Castillejo, Paolo M. Ossi, and Leonid Zhigilei, *Lasers in Materials Science*, Springer, 2014.
3 R. Dat, O. Auciello and A. I. Kingon, .
4 J.-P. Fang, J. Cai, Q. Wang, K. Zheng, Y.-K. Zhou and Z.-T. Geng, *Applied Surface Science*, 2022, **593**, 153436.
5 D. Kang, P. V. Pikhitsa, Y. W. Choi, C. Lee, S. S. Shin, L. Piao, B. Park, K.-Y. Suh, T. Kim and M. Choi, *Nature*, 2014, **516**, 222–226.
6 T. Yang, X. Li, X. Jiang, S. Lin, J. Lao, J. Shi, Z. Zhen, Z. Li and H. Zhu, *Mater. Horiz.*, 2016, **3**, 248–255.
7 C. Cho, P. Kang, A. Taqieddin, Y. Jing, K. Yong, J. M. Kim, M. F. Haque, N. R. Aluru and S. Nam, *Nat Electron*, 2021, **4**, 126–133.
8 N. Lambricht, T. Pardoen and S. Yunus, *Acta Materialia*, 2013, **61**, 540–547.
9 A. Vohra, K. Schlingman, R. S. Carmichael and T. B. Carmichael, *Chem*, 2018, **4**, 1673–1684.
10 Y. Ling, Q. Lyu, Q. Zhai, B. Zhu, S. Gong, T. Zhang, J. Dyson and W. Cheng, *ACS Sens.*, 2020, **5**, 3165–3171.
11 B. Zhang, J. Lei, D. Qi, Z. Liu, Y. Wang, G. Xiao, J. Wu, W. Zhang, F. Huo and X. Chen, *Adv. Funct. Mater.*, 2018, **28**, 1801683.
12 J.-Y. Noh, S.-H. Ha, G. R. Jeon and J.-M. Kim, *Composites Science and Technology*, 2022, **230**, 109738.
13 G. Chen, N. Matsuhisa, Z. Liu, D. Qi, P. Cai, Y. Jiang, C. Wan, Y. Cui, W. R. Leow, Z. Liu, S. Gong, K.-Q. Zhang, Y. Cheng and X. Chen, *Adv. Mater.*, 2018, **30**, 1800129.
14 J. Zhu, X. Wu, J. Jan, S. Du, J. Evans and A. C. Arias, *ACS Appl. Mater. Interfaces*, 2021, **13**, 38105–38113.
15 Z. Liu, D. Qi, P. Guo, Y. Liu, B. Zhu, H. Yang, Y. Liu, B. Li, C. Zhang, J. Yu, B. Liedberg and X. Chen, *Adv. Mater.*, 2015, **27**, 6230–6237.
16 S. Peng, S. Wu, Y. Yu, P. Blanloeuil and C. H. Wang, *J. Mater. Chem. A*, 2020, **8**, 20531–20542.
17 B. Feng, T. Sun, W. Wang, Y. Xiao, J. Huo, Z. Deng, G. Bian, Y. Wu, G. Zou, W. Wang, T. Ren and L. Liu, *Advanced Materials*, 2022, 2208568.
18 Z. Jiang, N. Chen, Z. Yi, J. Zhong, F. Zhang, S. Ji, R. Liao, Y. Wang, H. Li, Z. Liu, Y. Wang, T. Yokota, X. Liu, K. Fukuda, X. Chen and T. Someya, *Nat Electron*, 2022, **5**, 784–793.